Contributions to Mineralogy and Petrology (2026) 181:38
https://doi.org/10.1007/s00410-026-02314-z

ORIGINAL PAPER

Calibration of the Fe–Ir redox sensor at high pressure and the oxygen fugacity of laser heated diamond anvil cell experiments

S. Dominijanni[1,7] · D. J. Frost[1] · L. S. Dubrovinsky[1] · N. Miyajima[1] · E. Koemets[1,2] · G. Aprilis[1,3] · S. Chariton[1,4] · T. Fedotenko[1] · S. Khandarkhaeva[1] · C. Melai[1,5] · I. Koemets[1] · Z. Liu[1] · V. Cerantola[3,6] · A. Chumakov[3] · M. Hanfland[3] · V. Svitlyk[3] · A. D. Rosa[3] · C. A. McCammon[1]

Received: 1 August 2025 / Accepted: 11 March 2026 / Published online: 28 April 2026

Abstract

The Fe–Ir binary alloy has been calibrated up to 100 GPa as a part of a thermodynamic model (oxygen fugacity (f_{O_2}) sensor system) to monitor the redox conditions during high–pressure and high–temperature petrology experiments. The existing Fe–Ir activity–composition relations at 1 bar and ~473–2873 K have been updated by including the pressure dependence on the activity–composition relations. We calibrated the volume dependent interaction parameter W^V up to 61 GPa and extrapolated the Margules activity model (i.e., W^G_{Fe-Ir} and W^G_{Ir-Fe}) up to 100 GPa by combining the experimentally determined compressibility and compositional data of the alloy, with those of the end member phases in a thermodynamic model. We apply the newly calibrated redox sensor to oxygen fugacity determination during laser heated diamond anvil cell (LHDAC) experiments. In situ LHDAC experiments were performed up to ~61 GPa and ~2000 K. We tracked the f_{O_2} conditions in the DAC by reacting the powdered mixture during laser heating to form a Fe–Ir alloy (sliding redox sensor) and using high–resolution synchrotron Mössbauer Source spectroscopy, powder X–ray diffraction, X–ray absorption near–edge structure spectroscopy, analytical transmission electron microscopy, and chemical analyses down to the nanoscale. The inferred oxygen fugacities measured at the specific *P–T* conditions of the experiments are ~1 log unit below the iron–wüstite buffer, which is lower than estimates obtained with the existing model and compared to multi anvil experiments performed with the same starting mixture at similar *P–T* conditions.

Keywords Laser–heated diamond anvil cell · Oxygen fugacity · Iron oxidation state · Redox sensor · Fe–Ir binary system · Activity–composition relations

Communicated by Dante Canil.

✉ S. Dominijanni
serenadominijanni@cnr.it

[1] Bayerisches Geoinstitut, University of Bayreuth, Bayreuth, Germany

[2] Diamond House, Harwell Science and Innovation Campus, Fermi Ave, Didcot OX110DE, UK

[3] ESRF-The European Synchrotron, CS40220, 38043 Grenoble Cedex 9, France

[4] Center for Advanced Radiation Sources, The University of Chicago, Chicago, IL, USA

[5] Trinity College Dublin, The University of Dublin, College Green, Dublin 2, Ireland

[6] Department of Earth and Environmental Sciences, Università degli Studi di Milano-Bicocca, Milan, Italy

[7] Present address: Institute of Science, Technology and Sustainability for Ceramics (ISSMC) of the National Research Council (CNR), Via Granarolo 64, 48018 Faenza, RA, Italy

Introduction

Oxygen fugacity (f_{O_2}) strongly influences geochemical properties and processes of the mantle, such as the speciation of multivalent elements and global cycles of volatile elements (Frost and McCammon 2008). Because of its significance in governing a broad range of physicochemical processes involving solids, aqueous fluids, and melts in Earth's interior, any experimental system designed to simulate natural conditions requires internal measurement of f_{O_2}. Large volume presses (e.g., multi anvil, piston cylinder) have been used to perform experiments to investigate the effect of f_{O_2} in the shallow parts of the mantle. Indeed, despite the use of sintered diamond anvils that made it possible to simulate deep lower mantle pressures (up to ~ 100 GPa at high temperature; Zhai and Ito 2011 and references therein), most multi anvil presses are only able to reach conditions equivalent to those at the top of the lower mantle (~ 28 GPa; ≤2500 K). For these reasons, a thorough understanding of the complex redox processes occurring at pressures in the deepest portions of Earth's interior is still lacking.

In most experiments conducted at high pressure and high temperature using large volume presses, two main methods have been employed to either control or measure f_{O_2}: (i) calibrated solid assemblages that buffer f_{O_2} at specific values (Eugster 1957; Huebner and Sato 1970), or (ii) employ Fe–noble metal alloys as sliding redox sensors (Borisov and Palme 2000; Jamieson et al. 1992; Taylor et al. 1992; Woodland and O'Neill 1997). In the latter, the f_{O_2} of an experimental system can be determined from an equilibrium between either oxides or silicates containing a variably valent transition metal (usually iron) and a metallic alloy comprising the transition metal and a diluting noble metal (Woodland and O'Neill 1997), i.e.,

$$M\,(alloy) + (m/4)\,O_2 = MO_{m/2}\,(silicate/oxide) \quad (1)$$

where *m* indicates the valence state of the transition metal M (Borisov and Palme 2000; Woodland and O'Neill 1997). The alloy is composed of the metal M and a noble metal that might be, for example, Ir, or Pt, that is not oxidized in the equilibrium reaction and remains a metallic dilutant. If an f_{O_2} is imposed in a high temperature experiment, the composition of the alloy shifts, i.e. slides, to approach equilibrium with this f_{O_2} (Taylor et al. 1992). Following the experiment, the alloy composition can be used to estimate f_{O_2}; however, accurate determination requires chemical analyses and thermodynamic modeling not only of the alloy phase but also of the coexisting phases. This is necessary to constrain the chemical potential of the oxide component $\mu_{MO_{m/2}}$, particularly when phase activities deviate from unity. Normally a pure noble metal is added to the starting material and the alloy forms during the experiment through reduction of the transition metal from the silicate or oxide. Commonly employed redox sensors are face–centered cubic (*fcc* or γ) Pt–Fe (Hultgren et al. 1973), Pd–Fe (Hultgren et al. 1973; Tomiska 1989), and Ir–Fe (Schwerdtfeger and Zwell 1968; Swartzendruber 1984). A plausible choice of system can be made according to the criteria: (i) a continuous solid–solution series should be present at high temperature over the range that will be used in the experiment; (ii) the activity–composition relations for the system should be well defined over the chosen temperature interval; (iii) the oxide component should be insoluble in the metal phase and vice versa; (iv) no phase transitions should occur in the sensor materials. The Fe–Ir system has been considered among the most amenable because only one phase, γ–Fe–Ir, is stable over a wide temperature range for the entire compositional series (Swartzendruber 1984). The activity–composition relations and volume of mixing were investigated by Schwerdtfeger and Zwell (1968) at 1200 °C and 1 bar using a gas mixing furnace, and then further parametrized by Woodland and O'Neill (1997) and Stagno et al. (2013, 2015). However, knowledge of the pressure dependence of thermodynamic parameters for the Fe–Ir redox sensor is still lacking. The pressure dependence of activity–composition relationships, specifically the Margules parameters, can be independently determined from the excess volume of mixing. While the excess volume at 1 bar is often assumed to be a constant which is independent of pressure and temperature, this assumption becomes questionable at high pressures. With experimental techniques such as the diamond anvil cell capable of producing extreme pressures, it is likely that the excess volume does vary with pressure and should not be treated as invariant. To evaluate this, we have determined the effect of pressure on the excess volume and updated the existing thermodynamic model for the Fe–Ir redox sensor to enable f_{O_2} to be determined more accurately in high–pressure experiments.

Oxygen fugacity has only rarely been measured or controlled in the diamond anvil cell (Hirschmann and Zhang 2023). It is quite possible, for example, that contradictory results concerning whether $FeCO_3$ (Cerantola et al. 2017) or $CaCO_3$ (Dorfman et al. 2018) breakdown at lower mantle conditions, may well be explained by undetermined variations in experimental oxygen fugacity. We therefore applied the updated Fe–Ir redox sensor to determine the f_{O_2} in the laser–heated diamond anvil cell and performed complementary multi anvil experiments using the same starting mixture at similar experimental conditions for comparison.

Experimental procedures

Starting material

Starting materials consisted of polycrystalline and pre–synthesized ferropericlase plus iridium metal. Details of the ferropericlase synthesis are described in Longo et al. (2011) and briefly summarized here. Magnesium (Mg) and iron (Fe) metals were mixed in stoichiometric proportions to give a molar fraction of Fe of 25 mol %. To produce pure (Mg, Fe)O crystals, the metals were dissolved in HNO_3, the mixture was heated at 50 °C, and NH_4OH was added to the solution; excess HNO_3 and NH_4OH were removed by drying the obtained gel at temperatures of ~1200–1500 °C. A pressed pellet of this mixture was equilibrated in a gas-mixing furnace under CO/CO_2 at 1300 °C for 12 h at controlled oxygen fugacities (log f_{O_2} ranging from – 11 to – 7 log bar units). The sample was then quenched in water to prevent ferrite crystal formation (Longo et al. 2011). We confirmed the sample homogeneity and oxidation state of Fe using conventional Mössbauer spectroscopy at the Bayerisches Geoinstitut (Bayreuth, Germany). The fit of the Mössbauer spectrum showed $Fe^{3+}/\Sigma Fe$ of 12(2) % in ferropericlase, consistent with the known phase relations in the Mg–Fe–O system at 1 bar (e.g., Kang et al. 2000). No spinel–type phases were detected during measurements. Polycrystalline $(Mg_{0.75}Fe_{0.25})O$ was then ground with 5 mol % of reagent–grade iridium metal (99.999% purity) for about 1 h in an agate mortar under ethanol to achieve a homogeneous mixture. Notably, while this high Ir content was added to act as a redox sensor, it may influence phase relations in redox–sensitive systems. The mixed powder was used both for diamond anvil cell and multi anvil experiments to compare redox conditions achieved with both techniques. Table S1 shows an overview of all experimental conditions and spectroscopic analyses performed in this study, described in detail in the following paragraphs.

Diamond anvil cell experiments

An irregularly–shaped compressed pellet of starting powder (~60 µm long in the diagonal direction with thickness of ≤ 10 µm) was placed inside a drilled Re gasket hole (~100 µm diameter) pre–indented to a thickness of ~30 µm. The sample chamber was loaded with Ne as a quasi–hydrostatic pressure transmitting medium using the gas loading system installed at BGI (Kurnosov et al. 2008). We used piston–cylinder BX90 type DACs (Kantor et al. 2012) equipped with tungsten carbide seats and Boehler–Almax design anvils (Boehler and De Hantsetters 2007). Diamonds with culet sizes of 250 µm (runs SD001 and SD002) were used for high–pressure and high–temperature experiments. High pressures were generated by manually tightening the screws of the DACs in steps of ~5 GPa up to 36.0(5) GPa (SD001) and 61.5(1) GPa (SD002). After reaching the target pressure, samples were double–sided laser–heated at ~2000 K using a portable double–side pulsed laser heating system for about 20–30 min to ensure thermal equilibration. The laser setup was equipped with two IR ytterbium–doped fiber lasers (YLR–100–AC of IPG Photonics) that allow samples to be heated from both sides with a focal spot of ~10–15 µm and which operate at 1070 nm with a maximum power of 100 W (Aprilis et al. 2017, and references therein). Temperatures were measured during heating on both sides of the sample using spectroradiometry, and uncertainties are estimated to be about ±150 K due to possible temperature gradients and heating instability (Kantor et al. 2018).

Multi anvil experiment

The same starting powder was placed inside a folded Re foil capsule, with dimensions of ~2 mm in length and ~1 mm in diameter. Sample S7153 was synthesized at 26(1) GPa and 1973(353) K in a 1200–ton Kawai–type multi anvil press at BGI. The sample was held at the target temperature for one hour to ensure chemical homogeneity and equilibrium of crystallized phases (see Supplementary Information), consistent with multi anvil studies, such as Stagno et al. (2011), who used similar durations at 25 GPa and 1873 K. Tungsten carbide anvils of 3 mm truncation edge length were used with a 7 mm edge length Cr_2O_3–doped MgO octahedron (referred to as 7/3 assembly, see Fig. S1). High temperatures were reached by employing a $LaCrO_3$ heater and were monitored by a $W_{97\%}Re_{3\%}$–$W_{75\%}Re_{25\%}$ thermocouple (D–type) inserted horizontally through the wall of the furnace, directly in contact with the Re capsule. The recovered sample was mounted in epoxy resin, sectioned to expose the capsule material and polished for analysis. Afterwards, the sample was doubly polished to the optimal thickness (200 µm) according to the measured Fe content in ferropericlase and sample geometry for Mössbauer spectroscopy measurements.

Synchrotron powder X–ray diffraction (XRD)

Powder XRD experiments were conducted at the High–Pressure Diffraction Beamline ID15B (Merlini and Hanfland 2013) of the European Synchrotron Radiation Facility (ESRF). X–rays (λ = 0.411491 Å) were focused on an area of approximately 10 × 10 μm^2 FWHM vertically by a spherical mirror and horizontally by the Si (111) Laue monochromator installed on the optical table. A large area (430 × 350 mm) MAR555 flat panel detector was used for XRD data acquisition. Before the experiments, the

detector–sample distance was calibrated using CeO_2 reference material. The compressibility of ferropericlase and Fe–Ir alloy was investigated during decompression on both quenched SD001 and SD002 run products. We acquired XRD wide–scan images during continuous rotation of the DAC from –20° to +20° ω at each position of interest per pressure point (2 s of exposure time per degree of rotation). Additional XRD maps were acquired on experimental run SD002 at 61.5(1) GPa at the High– Pressure Beamline ID27 at ESRF (Perkin Elmer flat panel detector, λ = 0.3738 Å) to explore possible inhomogeneity after heating. We calculated pressures from the positions of the X–ray diffraction lines of Ne (Fei et al. 2007).

The resulting diffraction data were analyzed using the software DIOPTAS (Prescher and Prakapenka 2015) for phase identification, pressure estimation, and integration of both preliminary still images and wide–scan images. Le Bail data processing of integrated powder diffraction patterns was carried with the JANA2006 software (Petrícek et al. 2014) using manual background correction and pseudo-Voigt line shape.

Synchrotron Mössbauer source (SMS) spectroscopy

SMS spectra were recorded at the Nuclear Resonance Beamline (Potapkin et al. 2012; Rüffer and Chumakov 1996) ID18 of the European Synchrotron Radiation Facility using the (111) Bragg reflection of a $^{57}FeBO_3$ single crystal mounted on a velocity transducer (Wissel MVT–1000), which moves the crystal in the plane parallel to its surface (Potapkin et al. 2012). The high brilliance X–ray beam emitted by the SMS radiation was focused to 14 µm vertical and 13 µm horizontal dimensions using Kirkpatrick–Baez (KB) mirrors. The source linewidth was controlled before and after the acquisition of each SMS spectrum using a $K_2Mg^{57}Fe(CN)_6$ single line absorber. The velocity scale of all SMS spectra was calibrated relative to a 25 µm thick α–Fe foil. We collected SMS spectra of diamond anvil cell samples (SD001 and SD002) before (on the starting ferropericlase) and after laser heating, with acquisition times ranging from 1 to 2 h. Two SMS spectra were also acquired on multianvil run S7153 in different areas of the sample. All Mössbauer spectra were fitted using a full transmission integral with pseudo–Voigt line shape and 1st order polynomial baseline implemented in the MossA software package (Prescher et al. 2012).

X–Ray absorption near–edge structure (XANES) spectroscopy

Fe oxidation state in ferropericlase was also determined by X–ray absorption near edge structure (XANES) spectroscopy. XANES data acquisition was conducted at the energy–dispersive beamline ID24 of ESRF. The X– ray beam was focused horizontally at 4 µm FWHM employing an elliptically bent Si (311) crystal and vertically at 3 µm FWHM using a combination of Si mirrors in a KB configuration (Pascarelli et al. 2016). Pixel–energy calibration was performed using a reference α–Fe foil spectrum. XANES spectra were collected at the Fe *K*– edge at 7190 eV on the center position of sample SD002 after laser heating at 61.5(1) GPa.

We acquired XANES maps by scanning the DAC horizontally and vertically in steps of 5 µm in the focal plane of the X–ray beam (Fig. S2). Fe *K*–edge XANES were recorded over 6 (h) × 3 (v) step grids in order to cover an area of 450 μm^2. The resulting map contains 18 XANES spectra (Aquilanti et al. 2009). We selected the best heated/reacted area of the sample (white dashed rectangle in Fig. S2b) as the best representation of equilibrium. The data map was treated using the Region of Interest (ROI) Imaging Tool of the PyMCA software (Solé et al. 2007), which allows normalization and visualization of XANES spectra (one spectrum per pixel). The data were processed by subtracting a linear pre–edge background and normalizing the post–edge jump to unity (Fig. S2c).

Transmission electron microscopy (TEM)

Characterization of the sample from DAC experiments was performed using TEM due to the small size of crystallized phases after heating (a few microns on average) and the brittleness of the recovered material. We prepared a thin foil of sample SD001 using the focus ion beam instrument at BGI (FEI, Scios DualBeam) to enable TEM analysis on the best reacted area of the specimen. Firstly, the sample was carefully detached from the diamond anvil together with the Re gasket. Platinum rectangular layers were deposited by the Pt–GIS (Gas Injection System) needle at the sample/gasket boundary to ensure a solid connection between them before cutting (Fig. S3a). Due to the brittleness of the specimen, we placed an additional Pt bridge across the sample surface (Fig. S3b) to prevent potential sample loss during the FIB–cut. A Pt layer of ~ 20 µm length and ~ 1–2 µm thickness was also located transversely to the Pt bridge on top of the selected area of interest (white rectangle, Fig. S3c) where the foil was to be cut. The specimen was then tilted at ~ 52° and cut at the front and backside of the lamella by a scanning Ga ion beam (Fig. S3d,e) employing an acceleration voltage of 30 kV and a current of 0.3–30 nA (Miyajima et al. 2019; Wirth 2009). After completing the trenches (Fig. S3f), we tilted the stage at 7° and performed parallel milling to detach the foil from the sides and lift it out using a tungsten needle driven by a micromanipulator. The foil was

then attached to the copper grid (Fig. S3g) by platinum. At the final step after the energy dispersive X–ray spectroscopy (EDS) analysis in the FIB, the lamella was thinned down to 100 nm under low current conditions at the same voltage by tilting the stage at 57° and 47° to polish the front and back sides of the lamella, respectively, and reduce the effect of irregular topography and remove the surface contamination of hydrocarbon. EDS analysis was performed by turning the sample stage to zero degrees after completing the cutting procedure. Measurements were acquired with a silicon drift detector (SDD) employing an acceleration voltage of 20 kV. The ZAF correction was applied.

Quantitative energy dispersive X–ray microanalyses, electron energy–loss spectroscopy (EELS) measurements and microstructure textural observations were conducted on the extracted film (sample SD001) using a high–resolution transmission electron microscope (FEI Titan G2 80–200 S/TEM) equipped with an energy filter system, (Gatan Quantum SE) and operating at 200 kV. We mapped the Fe valence state in ferropericlase grains collecting Fe $L_{2,3}$–edge electron energy–loss near–edge structure (ELNES) spectra in scanning TEM (diffraction) mode under the following operating conditions: 2.5 mm EELS entrance aperture, illumination angle of $2\alpha = 14$ mrad, collection angle $2\beta = 17$ mrad, energy dispersion of 0.05 eV/channel, and 0.5 s of integration time per read–out (the total measuring time 0.5 s × 60 times = 30 s). The incident beam current was about 220 pA for the scanning TEM mode. We examined a total of 10 ferropericlase grains to explore potential variation in the Fe valence state and for good counting statistics. An EELS spectrum of the starting material was also acquired at the same operating conditions to compare the Fe^{3+} content in ferropericlase determined before and after LHDAC experiments. Data processing of the measured spectra included subtraction of the background intensity and a double Arctan–function (Van Aken et al. 1998). We quantified the Fe $L_{2,3}$–edge ELNES determining the integral Fe $L_{2,3}$–edge white–line intensity ratio $I(L_3)/I(L_2)$ as a function of the ferric iron concentration using the EELSA[1] software package, following the procedure described by Van Aken et al. (1998) and Van Aken and Liebscher (2002). Two integrated windows of 2 eV width were applied to the $L_{2,3}$ edges, from 708.5 to 710.5 eV and from 719.7 to 721.7 eV, centered around the maximum at the L_3 edge for Fe^{3+} and the L_2 edge for Fe^{2+}, respectively. The ferric/ferrous ratio in ferropericlase was calculated using an empirical universal curve calibrated for natural samples and solid solutions (Van Aken and Liebscher 2002).

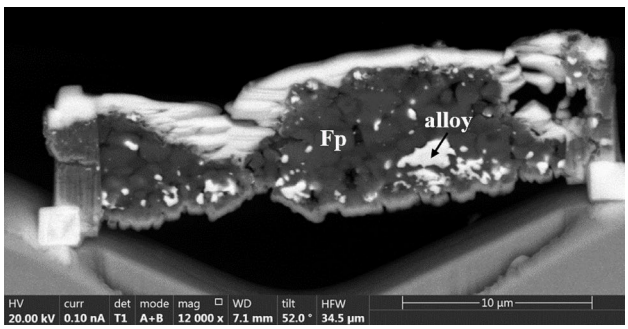

Fig. 1 Back–scattered electron (BSE) image of SD001 sample after FIB cross–section. The bright phase corresponds to Fe–Ir alloy, while the medium–grey phase represents ferropericlase.

Chemical analysis

Textural observation, preliminary phase identification and semi–quantitative chemical analysis of sample S7153 recovered from the multianvil experiment were conducted using a scanning electron microscope (SEM; ZEISS Gemini 1530) equipped with an energy dispersive X–ray spectrometer (EDXS) operating at 15 kV. Quantitative analysis of coexisting phases was performed using the electron microprobe (JEOL J–XA 8200) equipped with five wavelength dispersive spectrometers. We used an acceleration voltage of 20 kV and a beam current of 20 nA for alloy measurements (46 points), while for oxide analyses we set conditions to 15 kV and 15 nA (56 points). ZAF and phi–rho–Z matrix corrections were applied to metal and oxide phases, respectively. Instrument calibration was performed using in–house standards, i.e., Mg–enstatite, Fe–Fe metal, Ir–Ir metal.

Results and discussion

Chemical composition and iron oxidation state of Fe–Ir alloy and ferropericlase

Results of chemical analysis and textural observations conducted on the recovered FIB lamella of sample SD001 show the formation of Fe–Ir alloy through a redox reaction with ferropericlase after increasing pressure and temperature (Fig. 1). EDS chemical analyses collected on recovered FIB lamella during the cutting procedure are consistent with EDS measurements performed with the TEM within experimental uncertainty. The average mole fractions of Fe in the Fe–Ir alloy and FeO in ferropericlase were determined to be 0.42 ± 0.02 and 0.24 ± 0.04, respectively. TEM elemental mapping of Fe, Mg, and Ir on the recovered thin film further confirms the distribution of chemical elements across the sample surface (Fig. S4), with minor Si and Ca impurities likely originating from starting material contamination

[1] Program written by Clemens Prescher available at http://www.clemenspresher.com/programs/eelsa

during grinding. Laser heating in the DAC can potentially mobilize carbon from the diamond anvils and induce reactions with Fe (Aprilis et al. 2019). Although spectroscopic measurements did not indicate the presence of C–bearing Fe alloys, the lack of carbon standardization in EDS, FIB, and TEM analyses prevents a complete exclusion of trace carbon in the alloy. However, previous experimental studies on solid *fcc* noble metals, including iridium, show that carbon solubility is very low under equilibrium conditions (e.g., Arnoult and Mclellan 1972), with reported values on the order of 10^{-2} to 10^{-4} mol fraction for C in Ir, implying that any dissolved carbon in our Fe–Ir alloy would be at trace levels unlikely to significantly affect thermodynamic properties.

Detailed maps and point analysis results are provided in Table S3. Similar analyses on the multi anvil experiment (run S7153) confirm Fe–Ir alloy formation via reaction of Fe from ferropericlase with metallic Ir, with average Fe molar fractions of 0.14(1) in the alloy and 0.29(1) FeO in ferropericlase (Fig. S5).

The sample recovered from DAC experiment SD001 was analyzed using high–resolution Fe $L_{2,3}$–edge ELNES in EELS, XANES, and SMS spectroscopy. Quantitative EELS measurements on re–thinned specimen foils (~40 nm) from SD001 show spectra characteristic of divalent Fe, with negligible trivalent Fe (<5% according to Van Aken et al. 1998 and Van Aken and Liebscher 2002 methodology), in contrast to the starting ferropericlase powder which contains 6(5) % Fe^{3+} (Fig. S6). Given the associated uncertainties, the Fe^{3+} contents of the starting ferropericlase powder determined by Mössbauer spectroscopy and EELS are statistically consistent. Complementary *in situ* high–pressure XANES at the Fe *K*–edge on sample SD002 reveals that the rising edge energy position (7122.7 eV) overlaps with that of FeO standards, indicating ferropericlase is dominated by Fe^{2+} after laser heating (Fig. S7). The XANES spectra also display a feature at ~7144 eV, consistent with a high–spin to low–spin ($^{VI}Fe^{2+}$) spin crossover, corroborated by X–ray diffraction. SMS measurements further support these observations. For the DAC experiment, Mössbauer spectra of SD001 before laser heating show ~11(2) % Fe^{3+} at 36 GPa (Fig. 2a), while spectra after laser heating were interpreted by assigning singlets to Fe metal in the Fe–Ir alloy (Fig. 2b, c), as EELS and XANES confirmed negligible Fe^{3+} content. In general, laser heating caused the sample to become more reduced, as indicated by the decreased $Fe^{3+}/\Sigma Fe$ ratio in ferropericlase and the partial reduction of FeO to metallic iron, which was subsequently incorporated into Fe–Ir alloys. Trace amounts of adsorbed water in the starting materials likely facilitated this reduction by coupling it to oxidation reactions involving either the Re gasket or the diamond anvils.

At 61.5(1) GPa, a new spectral component corresponding to low–spin $^{VI}Fe^{2+}$ appears in both DAC and multi anvil experiments (Fig. 2b–d). The relative area of Fe metal in the alloy is lower in the multi anvil experiment due to the smaller Fe fraction in the alloy, consistent with the compositional data discussed above. Detailed SMS results are provided in Table S2 of the Supplementary Information.

XRD analysis and equations of stat

Synchrotron powder X–ray diffraction measurements on the diamond anvil cell samples show the formation of Fe–Ir alloy with *fcc* structure following the reaction of Ir metal and Fe from ferropericlase. Figure 3 illustrates a comparison between integrated diffraction patterns collected before (green) and after (red) laser heating at 11.0(5) GPa. Calculated intensity XRD profiles were obtained after performing Le Bail data processing. All quenched XRD patterns exhibit disappearance of Ir peaks indicating complete reaction of Ir metal to form Fe–Ir alloy as well as confirming the homogeneity of laser heating (magnified Fig. 3b). Analysis of diffraction data at different pressures showed that all quenched diffraction patterns can be indexed with three phases, i.e., ferropericlase, Ne, and Fe–Ir alloy with *fcc* structure and Fm $\bar{3}$m space group. The newly crystallized Fe–Ir alloy maintains the *fcc* structure over the entire investigated pressure range (up to 61.5(1) GPa). An example of an XRD pattern collected at the highest pressure after cooling is shown in Fig. S8. Pressure dependence of volume parameters for Fe–Ir alloy and ferropericlase (run SD002) were fit with a third–order Birch–Murnaghan (BM3) EOS using the EosFit7–GUI software (Angel et al. 2014; Gonzalez-Platas et al. 2016) and are shown in Figs. S9 and S10 with the corresponding F–*f* plots. All *V(P)* data were collected at 300 K under quasi-hydrostatic conditions, without reannealing during either compression or decompression. Figure 4a shows the *P–V* relationship for Fe–Ir determined in this study as well as the predicted ideal behaviour compared with those of the end member phases, pure *fcc* Fe (Campbell et al. 2009) and *fcc* Ir (Yusenko et al. 2019) reported in selected previous work. Unit cell lattice parameters of *fcc* Fe (Fig. S9) are related to high–temperature measurements (i.e., 1273 K; Nishihara et al. 2012, and ~1300–2700 K; Komabayashi et al. 2009) since at room temperature and high–pressure Fe is known to assume the *hcp* structural phase (see, for example, Tateno et al. 2010). The calculated EOS curve for Fe–Ir alloy shows no evidence of pressure–induced phase transitions over the investigated pressure range. Fits of the third–order Birch-Murnaghan equation of state to pressure–volume data yielded K_{T0} = 356±11 GPa, K'_{T0} = 2.3±0.3, and V_0 = 53.97±0.06 Å^3. A comparison between EOS coefficients of the Fe–Ir alloy determined in this study with those of the

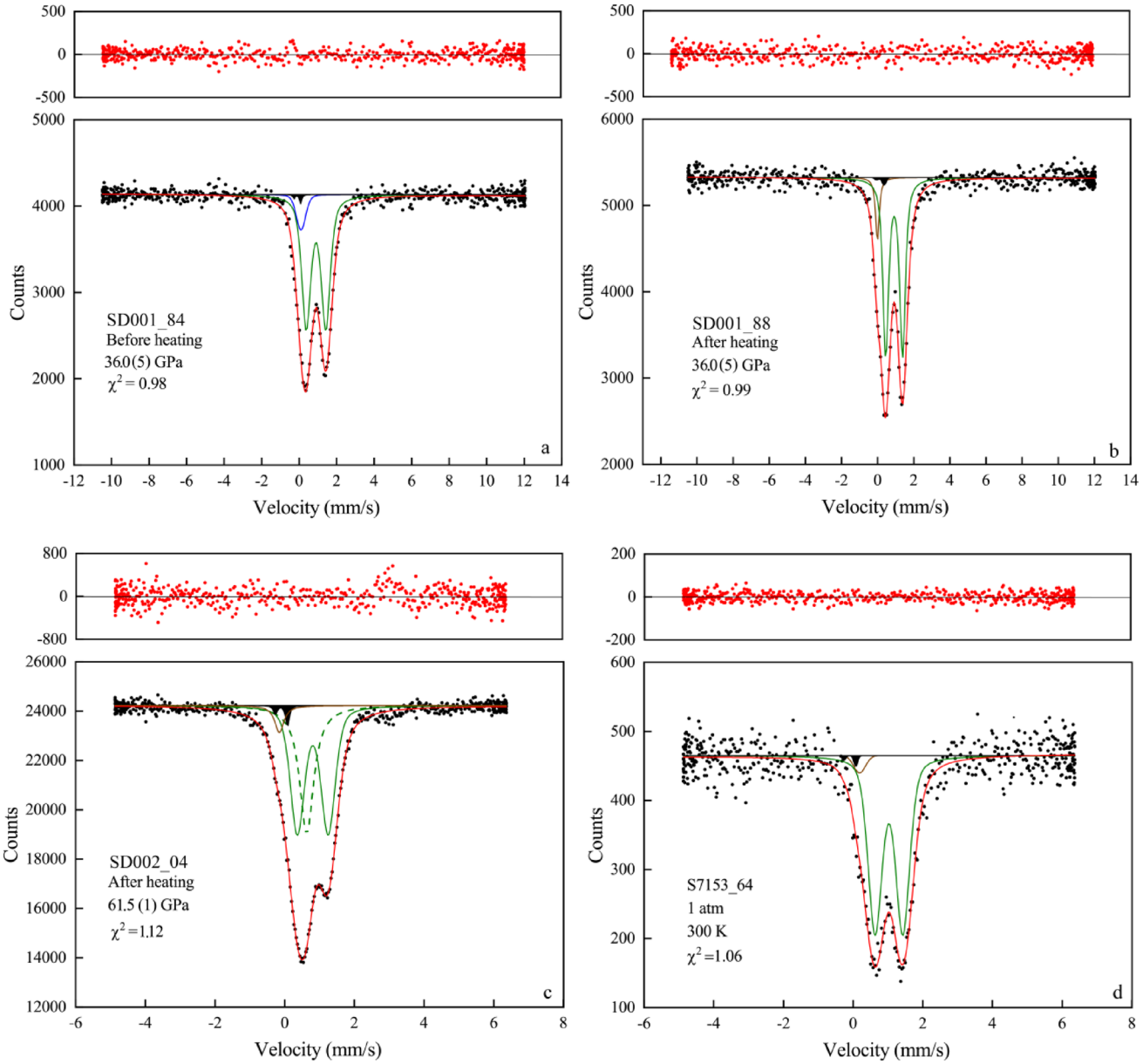

Fig. 2 Room temperature Mössbauer spectra of **a** the starting material ($Fe^{3+}/\Sigma Fe = 11(2)$ %); **b** the same material after laser heating in the diamond anvil cell at 36.0(5) GPa ($Fe^{3+}/\Sigma Fe$ = not detected) and **c**) 61.5(1) GPa ($Fe^{3+}/\Sigma Fe$ = not detected); **d** sample S7173 recovered to room pressure from a multi anvil experiment ($Fe^{3+}/\Sigma Fe$ = not detected). In all spectra, solid circles (black) are experimental data, solid curves (red) represent the total fit performed with pseudo-Voigt functions, solid doublets (green) are high–spin Fe^{2+} absorption, and singlet features are either Fe^{3+} in ferropericlase (blue—part **a**) or Fe^0 in Fe–Ir alloy (brown—parts **b**–**d**). Spectra acquired at 61.5(1) GPa show the appearance of a new spectral component (dashed green singlet—part **c**) representing low–spin Fe^{2+} absorption. An asymmetric doublet was added to the fit of all spectra (solid black) to account for the Fe contribution in the Be lenses in the optics of the ID18 beamline. The residual is shown in red above each spectrum. The velocity scale is relative to α–Fe at ambient conditions.

end member phases (i.e., metallic *fcc* Fe and Ir from the literature) is given in Table S4, respectively. The relatively high value of K_{T0} obtained for the Fe–Ir alloy is consistent with its Ir–rich composition, as Ir is among the least compressible transition metals and therefore contributes strongly to the stiffness of the solid solution. However, the unusually low value of K'_{T0} is not expected from compositional effects alone. Instead, this parameter combination reflects the well–known covariance between K_{T0} and K'_{T0} inherent in the third–order Birch–Murnaghan EOS (e.g., Angel et al. 2014). Over the modest pressure range and limited volume compression achieved in this study, the curvature of the *P–V* data is only weakly resolved, allowing the BM3 fit to trade a lower K'_{T0} for a correspondingly higher K_{T0} without significantly altering the quality of the fit. This behavior is also evident in the associated *F–f* plot (Fig. S9b), which

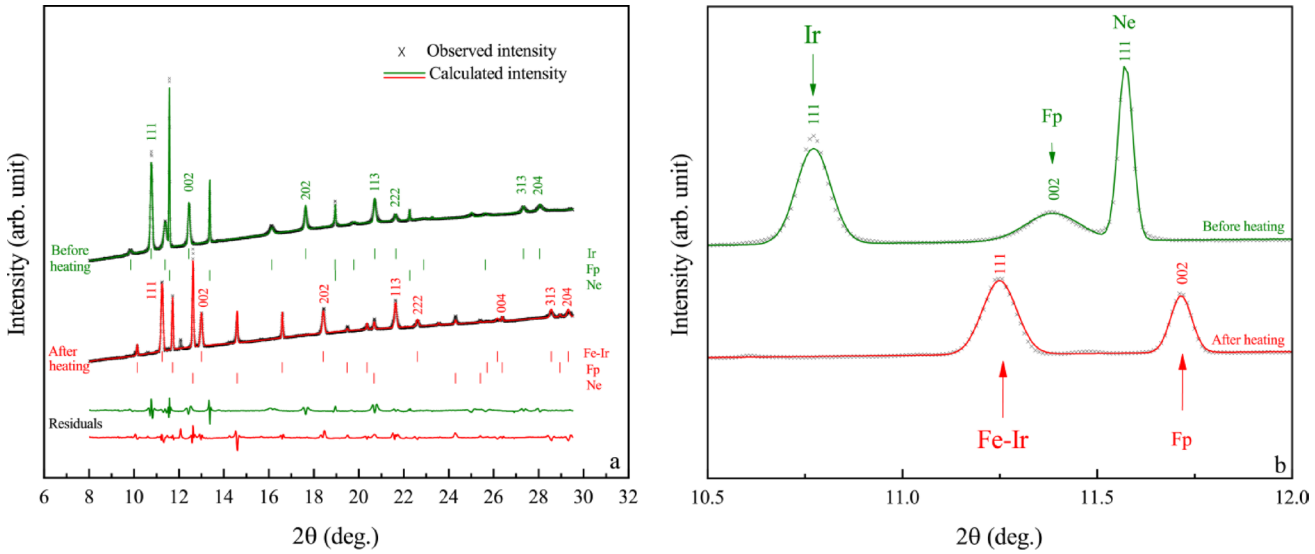

Fig. 3 **a** Comparison of XRD patterns collected at 11.0(5) GPa and 300 K on sample SD001 before (green) and after (red) laser heating. Identified phases before heating are ferropericlase, Ne (pressure transmitting medium) and Ir metal. After quenching a Fe–Ir alloy is formed by the reaction of Ir metal and Fe from ferropericlase; **b** magnified image illustrates the vanishing of Ir peak after laser heating and appearance of the Fe–Ir diffraction peak. Le Bail refinement was performed using Jana software package (Petrícek et al. 2014).

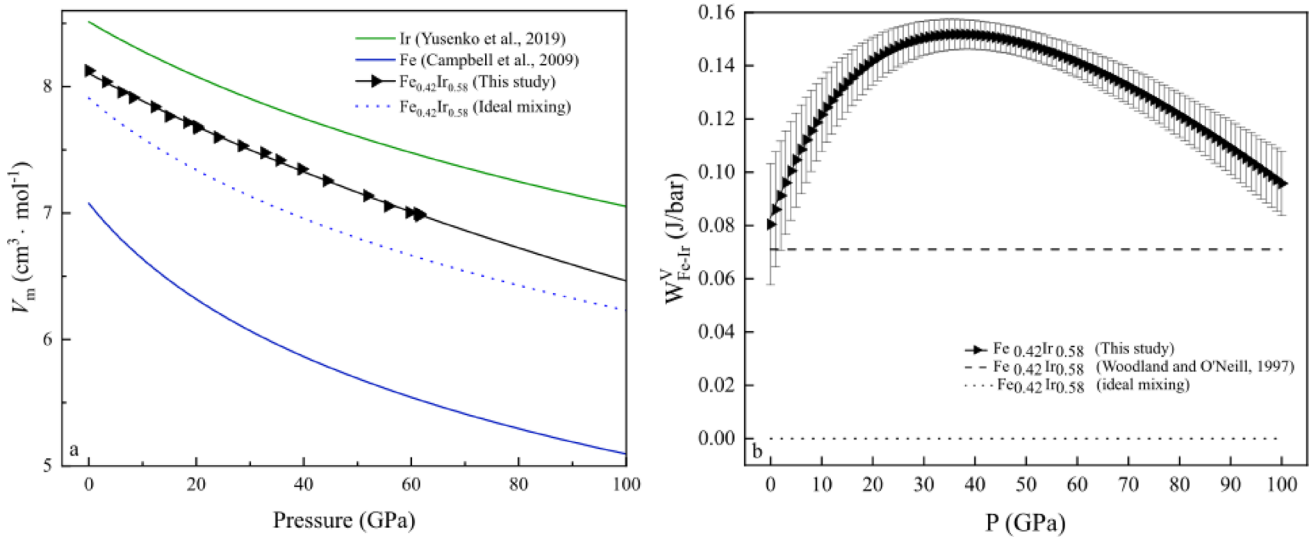

Fig. 4 **a** Volume of *fcc* Fe–Ir alloy at 300 K collected for run SD002, compared with previous *P–V (–T)* equations of state for pure *fcc* Ir (green; Yusenko et al., 2019) and *fcc* Fe (blue; Campbell et al., 2009). Black triangles indicate *fcc* Fe–Ir data from this study, and the black line represents the least-squares fit to an isothermal third-order Birch–Murnaghan equation of state. The blue dotted curve represents the ideal mixing of a $Fe_{0.42}Ir_{0.58}$ alloy and is shown for comparison;**b** Volume-dependent Margules parameter as a function of pressure. The solid black line shows a 4th order polynomial fit to the data.

exhibits a modest negative slope consistent with $K'_{T0} < 4$, but with an overall magnitude that remains small relative to the uncertainties and the span of the dataset. Such conditions commonly lead to underestimated values of K'_{T0} and inflated K_{T0} when the second–order curvature term of the EOS is insufficiently constrained. Details of the compressibility of ferropericlase, including the derived BM3 EOS parameters and corresponding *F–f* plots, are provided in the Supplementary Information (Fig. S10; Table S5).

Thermodynamic model

Oxygen fugacity calculations using the Fe–Ir redox sensor for our experimental assemblage use the equilibrium,

$$\underset{\text{alloy}}{2\text{Fe}} + \text{O}_2 = 2\,\underset{\text{Fp}}{\text{FeO}} \tag{2}$$

and,

$$\log(fo_2) = \frac{-\Delta_r G^{\circ}_{P,T}}{\ln(10)RT} + 2\log a^{Fp}_{FeO} - 2\log a^{alloy}_{Fe} \quad (3)$$

where $a^{\mathrm{Fp}}_{\mathrm{FeO}}$ and $a^{\mathrm{alloy}}_{\mathrm{Fe}}$ are the activities of FeO and Fe in the ferropericlase and alloy solutions respectively, R is the gas constant and $\Delta_{\mathrm{r}}\mathrm{G}^{\circ}_{P,T}$ is the standard Gibbs free energy of the reaction (2) between the endmembers determined using the following expression (e.g., Cemic 2005),

$$\Delta_r G^{\circ}_{T,P} = \Delta_r H(1bar,T) - T\Delta_r S(1bar,T) + \int_{1bar}^{P} \Delta_r V(P,T)\cdot dP \quad (4)$$

$\Delta_r H(1bar,T)$ and $\Delta_r S(1bar,T)$ are the enthalpy and entropy of the reaction calculated using the Holland and Powell data base (Holland and Powell 1998, 2011; Table 1). The $\Delta_r G^{\circ}{}_{T,P}$ value of the end member equilibrium cancels out when $\log(fo_2)$ values are normalised to IW. The $a^{\mathrm{Fp}}_{\mathrm{FeO}}$ and $a^{\mathrm{alloy}}_{\mathrm{Fe}}$ terms in Eq. (3) are calculated from the respective mole fractions, X, of each component using,

$$a_{FeO^{Fp}} = X^{Fp}_{FeO}.\gamma^{Fp}_{FeO} \quad (5)$$

$$a^{alloy}_{Fe} = X^{alloy}_{Fe}.\gamma^{alloy}_{Fe} \quad (6)$$

where $\gamma^{\mathrm{Fp}}_{\mathrm{FeO}}$ and $\gamma^{\mathrm{alloy}}_{\mathrm{Fe}}$ are the activity coefficients, described using symmetric (Eq. 7) and asymmetric (Eq. 8) Margules binary solution formalisms respectively (Thompson and Waldbaum 1969) as follows:

$$RT\ln\gamma^{Fp}_{FeO} = (1-X_{FeO})^2\cdot W^{Fp}_{FeO-MgO} \quad (7)$$

$$RT\ln\gamma^{alloy}_{Fe} = (1-X_{Fe})^2\left[W^{G}_{Fe-Ir} + 2X_{Fe}\left(W^{G}_{Ir-Fe} - W^{G}_{Fe-Ir}\right)\right]. \quad (8)$$

$W^{\mathrm{Fp}}_{\mathrm{FeO-MgO}}$ is a symmetric FeO–MgO interaction parameter for stoichiometric ferropericlase while $W^{G}_{\mathrm{Fe-Ir}}$ and $W^{G}_{\mathrm{Ir-Fe}}$ are asymmetric interaction parameters for the alloy. The interaction parameters can also vary as a function of temperature and pressure according to:

$$W^G = W^H - TW^S + PW^V \quad (9)$$

For ferropericlase these terms are taken from the literature (Frost 2003; O'Neill et al. 2003). For the Fe–Ir alloy, W^H can be fit to the activity–composition relations of Schwerdtfeger and Zwell (1968). In the absence of data to the contrary most studies have assumed W^S to be negligible (Stagno et al. 2011; Woodland and O'Neill 1997), although this should probably be further investigated in the future. W^V, which is often reported in J/bar (=$\mathrm{cm}^3\cdot\mathrm{mol}^{-1}$/10), can be independently determined from the excess volume of mixing $\Delta_m V^{ex}$, defined as,

$$\Delta_m V^{ex} = V_{Fe-Ir} - \left(X^{Pure}_{Fe}\cdot V^{Pure}_{Fe} + X^{Pure}_{Ir}\cdot V^{Pure}_{Ir}\right) \quad (10)$$

where $V_{\mathrm{Fe-Ir}}$ is the molar volume of the Fe–Ir alloy for a given composition and $X^{\mathrm{Pure}}_{\mathrm{Fe}}$ / $X^{\mathrm{Pure}}_{\mathrm{Ir}}$ and $V^{\mathrm{Pure}}_{\mathrm{Fe}}$ /$V^{\mathrm{Pure}}_{\mathrm{Ir}}$ are the molar fraction and molar volume of the pure endmembers of the alloy. Our estimated molar volume (8.104(1) $\mathrm{cm}^3\cdot\mathrm{mol}^{-1}$) and $\Delta_m V^{ex}$ (0.20(2) J/bar) for the $\mathrm{Fe}_{0.42}\mathrm{Ir}_{0.58}$ alloy at room conditions (i.e. 298 and 1 bar; Fig. S11) are in good agreement with existing data on Fe–Ir alloys reported for a wide compositional range (Schwerdtfeger and Zwell 1968; Stagno et al. 2015) that support a broadly symmetric excess volume of mixing. This symmetric excess molar volume of mixing can be described using a single fitting term, which is also the volume–dependent interaction parameter $W^{V}_{\mathrm{Fe-Ir}}$ i.e.,

$$\Delta_m V^{ex} = X^{Fe-Ir}_{Fe}\cdot X^{Fe-Ir}_{Ir}\cdot W^{V}_{Fe-Ir} \quad (11)$$

$W^{V}_{\mathrm{Fe-Ir}}$ can then be determined from:

$$W^{V}_{Fe-Ir} = \frac{\Delta_m V^{ex}}{\left(X^{Fe-Ir}_{Fe}\cdot X^{Fe-Ir}_{Ir}\right)} \quad (12)$$

Generally, the 1 bar value of $\Delta_m V^{ex}$ would be used in calculations that require high pressure estimates of W^G, however, if we are to employ the redox sensor at lower mantle conditions we can no longer ignore the fact that $\Delta_m V^{ex}$ likely also changes with pressure. To fully account for the effect of pressure on the thermodynamic mixing properties of the Fe–Ir alloy, we can take account of the compressibility behavior of the alloy, obtained by X–ray diffraction. To determine $\Delta_m V^{ex}$ at high pressure, we compared the unit cell volume of our alloy composition with pure Fe and Ir equations of state from previous studies (Campbell et al. 2009; Yusenko et al. 2019) up to 100 GPa. Figure S12 shows the isothermal bulk modulus K_{T0} of $\mathrm{Fe}_{0.42}\mathrm{Ir}_{0.58}$ alloy

Table 1 End member thermodynamic data used to calculate oxygen fugacity

	a	b	c	d	S_{298}	$\Delta_f H^{\circ}_{298}{}^{*}$	$K_{T0}{}^{*}$	$K'_{T0}{}^{*}$	V^{*}
	JK^{-1}	JK^{-2}	JK	$\mathrm{JK}^{-0.5}$	(J/K mol)	(J/mol)	GPa	GPa	$\mathrm{cm}^3\mathrm{mol}^{-1}$
Fe (*fcc*)	46.2	0.00516	723,100	–556.2	27.09	0	133(3)	5	7.076
FeO	44.4	0.00828	–1,214,200	185.2	60.6	–271,970	146.9(1.3)	4	12.26
O_2	48.3	0.00069	499,200	–420.7	205.2	0	–	–	

All thermodynamic parameters are taken from the Holland and Powell (1998, 2011) database

*Campbell et al. (2009)

Table 2 A comparison of experimental fo_2 estimates using previous and current models

Run	P (GPa)	T (K)	X_{Fe}^{alloy}	X_{FeO}^{Fp}	W_{Fe-Ir}^{G}(J/mol)	W_{Ir-Fe}^{G}(J/mol)	W_{Fe-Ir}^{V}(J/bar)	$W_{FeO-MgO}^{Fp}$(J/mol)	logfo_2	logfo_2[IW]
SD001	36.0(5)	2000	0.42(2)	0.24(4)	–51814[a]	–62769[a]	0.0736[a]	11000[b]	**–5.8(4)**	0.9(4)
SD001	36.0(5)	2000	0.42(2)	0.24(4)	**–2819(143)**	**–13,801(143)**	**0.15(6)**	**14960[b]**	**–6.8(4)**	**0.2(4)**
SD002	61.5(1)	2000	0.42(2)	0.24(4)	–51814[a]	–62769[a]	0.0736[a]	11000[b]	**–5.8(4)**	0.9(4)
SD002	61.5(1)	2000	0.42(2)	0.24(4)	**34,247(659)**	**23,265(659)**	**0.14(5)**	**17710[b]**	**–7.4(4)**	**-0.4(4)**
S7153	26(1)	2000	0.14(1)	0.29(1)	–51814[a]	–62796[a]	0.0736[a]	11000[b]	**–3.7(4)**	3.0(4)
S7153	26(1)	2000	0.14(1)	0.29(1)	**–17,974(66)**	**–28,956(66)**	**0.29(1)**	**13860[b]**	**–5.2(4)**	**1.8(4)**

Numbers in parenthesis are standard deviations of the last digit

[a]Values at 1 atm from Stagno et al. (2015) and Schwerdtfeger and Zwell (1968)

[b]Values from Frost (2003) and O'Neill et al. (2003)

Values in bold are parameters at high pressure

compared to those determined for Fe (e.g., Campbell et al. 2009) and Ir (Yusenko et al. 2019) pure endmembers. The Fe–Ir compressibility–composition relation positively deviates from the K_{T0}–X_{Fe} ideal mixing of the pure components, showing additional evidence for a non–ideal property of the binary solid solution.

Figure 4b displays the obtained $W_{\mathrm{Fe-Ir}}^{V}$ up to 100 GPa. To include the pressure effect on the $W_{\mathrm{Fe-Ir}}^{G}$ and $W_{\mathrm{Ir-Fe}}^{G}$ parameters, we fitted the high pressure $W_{\mathrm{Fe-Ir}}^{V}$ parameters using a 4th order polynomial function (black line Fig. 4b),

$$\left(W_{Fe-Ir}^{V}\right)_{fit} = ax^4 + bx^3 + cx^2 + dx + e. \tag{13}$$

A polynomial formalism was adopted for the excess volume term W^V because it provides an adequate description of the experimental data and allows the forward calculation of volume to be performed analytically, without the need for iterative numerical methods.

The asymmetric interaction parameters were corrected for the pressure by adding the newly determined integral of $W_{\mathrm{Fe-Ir}}^{V}$ as follows,

$$\left(W_{Fe-Ir}^{G}\right)_{P} = \left(W_{Fe-Ir}^{H}\right)_{1bar} + \int_{1bar}^{P} \left(W_{Fe-Ir}^{V}\right)_{fit} \cdot dP \tag{14}$$

$$\left(W_{Ir-Fe}^{G}\right)_{P} = \left(W_{Ir-Fe}^{H}\right)_{1bar} + \int_{1bar}^{P} \left(W_{Fe-Ir}^{V}\right)_{fit} \cdot dP. \tag{15}$$

These fully pressure dependent Margules parameters are then used in Eq. 8.

Experimental oxygen fugacity calculations

We evaluated the effect of the new pressure–corrected Fe–Ir thermodynamic model on fo_2 estimates for DAC and multi anvil experiments. Calculations based on the previous 1 bar model (Stagno et al. 2015; Swartzendruber 1984) were compared with results from the updated calibration, which accounts for pressure–dependent interactions. The updated model consistently predicts lower fo_2 values at high pressure, with differences exceeding 1 log unit, indicating that neglecting pressure effects can lead to systematic overestimation under extreme conditions. Table 2 lists the fo_2 results along with the high–pressure interaction parameters determined in this study, while the complete set of thermodynamic variables is provided in the supplementary information (Excel file). Uncertainties were propagated through the activity–composition relationship. Figure 5 compares absolute oxygen fugacities from multi anvil and DAC experiments using the previous model (dotted and dot–dashed

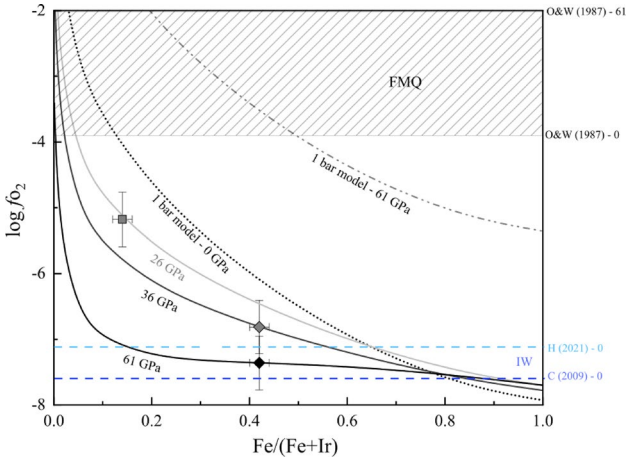

Fig. 5 Absolute oxygen fugacity as a function of Fe–Ir solid-solution composition in equilibrium with ferropericlase. Black dotted and grey dash–dotted curves show results from the existing redox sensor thermodynamic model (1 bar model; Stagno et al., 2015) at ambient pressure and 61 GPa, respectively. These are compared with log f_{O_2} values from the pressure–dependent updated model (grey and black symbols of this study) for multi anvil experiments (squares; X_{Fe}^{alloy} = 0.14, X_{FeO}^{Fp} = 0.29) and DAC experiments (diamonds; X_{Fe}^{alloy}=0.42, X_{FeO}^{Fp}=0.24). Blue and sky–blue dashed lines represent buffer equilibria calculated at 0 GPa and 2000 K from Campbell et al. (2009; blue dashed line, C-2009) and Hirschmann et al., (2021; sky-blue dashed line, H-2021). IW buffer equilibria at 61 GPa plot outside the displayed range, at log $f_{O_2} \approx -8$. The inclined shaded region represents the FMQ buffer calculated at 0 and 61 GPa after O'Neill & Wall (1987).

curves; 1 bar model of Stagno et al. 2015) and the updated calibration (solid black and gray curves; this study). Oxygen fugacities calculated at the specific experimental conditions with the updated activity model are lower by over 1 log unit compared to those estimated with the existing Fe–Ir sliding redox sensor, with f_{O_2} becoming more reducing with increasing pressure (the difference reaches 1.6 log units at 61 GPa, see Table 2). This discrepancy suggests that the new calibration affects the stability of redox sensitive phases, including C– and Fe–bearing minerals and melts. Previous f_{O_2} estimates based on the 1 bar model may therefore require revision. For example, Stagno et al. (2011) determined the oxygen fugacity at which magnesite ($MgCO_3$) is reduced to diamond in a typical peridotitic mantle assemblage, conducting high–pressure, high–temperature experiments (16–45 GPa and 1500–1700 °C) to constrain the stability of magnesite as a function of f_{O_2}. In those experiments, performed using a multi anvil press, oxygen fugacity was measured with an Fe–Ir redox sensor calibrated using the 1 bar thermodynamic model of Swartzendruber (1984). Since carbonate stability in Earth's mantle is highly sensitive to redox conditions (Cerantola et al. 2017; Dorfman et al. 2018; Rohrbach and Schmidt 2011; Stagno et al. 2011), the inferred stability field of magnesite depends directly on the estimated f_{O_2}.

Our recalibration of the Fe–Ir sensor indicates that the f_{O_2} conditions of these experiments are approximately one log unit lower than previously estimated at 45 GPa and 1700 °C. Re–evaluating the experiments under these revised redox conditions shifts the inferred stability field of magnesite to higher pressures than originally proposed. Under these conditions, the predicted f_{O_2} trajectory approaches the IW buffer (Campbell et al. 2009; Hirschmann 2021) near 45 GPa, suggesting that magnesite may coexist with diamond and C–bearing Fe metal at depths of approximately 1100 km.

Overall, the updated Fe–Ir calibration provides a more accurate representation of oxygen fugacity at high pressure and underscores the importance of incorporating pressure effects into redox sensor models. Moreover, the f_{O_2} results determined in this study for DAC experiments are more reducing compared to those measured during the multi anvil experiment, which is consistent with the use of Re as a capsule material.

Chemical equilibrium and redox measurements in LHDACs

The introduction of an oxybarometer for LHDAC experiments opens the possibility to directly measure the redox state of mineral phases and to probe volatile speciation at extremely high pressures and temperatures, simulating conditions beyond the capabilities of the multi anvil press down to the lower portion of the lower mantle. Typically, f_{O_2} is neither fixed nor controlled in LHDAC experiments. Only a few studies have reported to have controlled the f_{O_2} in DAC using redox buffer equilibria (e.g., Campbell et al. 2009; Shen et al. 2020; Shofner et al. 2016) but so far to our knowledge, there are no direct f_{O_2} measurements during *in situ* laser heating experiments with the redox sensor method. One possible reason for this are limitations (i.e., thermal gradient, different diffusion rate of the components, or stress distribution) in the achievement of chemical equilibrium. However, during the last two decades rapid evolution of DAC technology coupled with laser heating systems and synchrotron light sources (e.g., Anzellini and Boccato 2020) have enabled many of the previous challenges to be overcome.

In large–volume presses, equilibrium is often confirmed through "reversal experiments", where a phase boundary is bracketed by approaching it from both sides of the reaction path. However, diamond–anvil cell (DAC) experiments pose unique challenges–such as steep pressure gradients, extremely small sample volumes, and the difficulty of inverting reaction trajectories—making traditional reversal methods potentially unsuitable in this context. Instead, to evaluate equilibrium in our DAC runs, we complemented mineralogical phase characterization (see Methods section) with: (i) reproducibility across multiple runs; (ii) evidence of recrystallization in the most uniformly heated area; and (iii) confirmation of minimal temperature gradients via XRD and nanoscale analyses. Based on these criteria, we conclude that equilibrium was achieved in our experiments.

Conclusions

In this study we calibrated the Fe–Ir redox sensor at high pressure by including the effect of pressure on the excess volume dependency of the activity composition–relations up to 100 GPa. Our results provide a more accurate method for calculating the oxygen fugacity using this sensor and show that the application of the 1 bar excess volume to high pressure conditions can lead to overestimates in f_{O_2} calculations. The calibration of the Fe–Ir redox sensor at high pressure was conducted by determining the compressibility of a single intermediate alloy composition (i.e., $Fe_{0.40}Ir_{0.60}$) and comparing this with the end member phases. In order to ensure that the calculated excess volumes are well modelled, further intermediate compositions should be tested such as $Fe_{0.20}Ir_{0.80}$, $Fe_{0.60}Ir_{0.40}$, $Fe_{0.80}Ir_{0.20}$. A similar experimental strategy could be extended to the Fe–Pt and Fe–Pd systems, often employed as sliding redox sensors (Hirschmann and Zhang 2023). Testing the applicability of this newly

calibrated oxybarometer and evaluating the oxygen fugacity variation in laser heated DAC experiments was an additional focus of this study. We found that the oxygen fugacity in the DAC is lower than that determined for multi anvil experiments performed at comparable experimental conditions (i.e., 26 GPa and 36 GPa) and employing the same starting material. We further observed reducing conditions in the DAC from EELS, XANES, and SMS spectroscopies that showed negligible ferric iron in ferropericlase. The inferred oxygen fugacities measured at the specific *P–T* conditions of the experiments are lower than estimates obtained with the existing 1 bar model. The approach proposed in this study is a first step in considering the diamond anvil cell as a petrological tool to investigate mantle redox state at the extreme conditions of Earth's interior and provides a new method to calculate oxygen fugacity at high pressure.

Supplementary Information The online version contains supplementary material available at https://doi.org/10.1007/s00410-026-02314-z.

Acknowledgements This project was conducted under the "Deep volatile cycles – International Research Training Group" funded by German Research Foundation Deutsche Forschungsgemeinschaft – DFG, GRK 2156/1) and DFG grant FR1555/11. The authors acknowledge the CarboPaT research group (DFG FOR2125) for fruitful discussion on the dataset and thank D. Krausse for assistance during EMPA measurements, R. Njul for aid with sample preparation and T. Boffa Ballaran for help with XRD data interpretation. We acknowledge the European Synchrotron Radiation Facility for provision of synchrotron radiation facilities (ID15b, ID18, ID24 and ID27). We also acknowledge the DFG for funding of the FIB facility (Project number 257745926) and the TEM facility (Project number 189856261).

Author contributions S. Dominijanni: Writing—original draft; Writing—review & editing; Methodology; Investigation; Formal analysis; Data curation. C. A. McCammon: Conceptualization; Writing—original draft; Writing—review & editing; Visualization; Validation; Supervision; Resources; Project administration; Methodology; Investigation; Funding acquisition; Formal analysis; Data curation. D. J. Frost: Conceptualization; Writing—review & editing; Visualization; Validation; Supervision; Resources; Project administration; Methodolgy; Investigation; Funding acquisition; Formal analysis; Data curation L. S. Dubrovinsky: Writing—review & editing; Validation; Supervision, Methodology; Investigation; Formal analysis; Data curation N. Miyajima: Writing—review & editing; Validation; Supervision, Methodology; Investigation; Funding acquisition; Formal analysis; Data curation. E. Koemets: Methodology; Investigation; Formal analysis; Data acquisition and curation. G. Aprilis: Methodology; Investigation; Formal analysis; Data acquisition and curation. S. Chariton: Methodology; Investigation; Formal analysis; Data acquisition and curation; T. Fedotenko: Methodology; Investigation; Formal analysis; Data acquisition and curation. S. Khandarkhaeva: Methodology; Investigation; Formal analysis; Data acquisition and curation. C. Melai: Methodology; Investigation; Formal analysis; Data acquisition and curation I. Koemets: Methodology; Investigation; Formal analysis; Data acquisition and curation. Z. Liu: Methodology; Investigation; Formal analysis; Data acquisition and curation. V. Cerantola: Methodology; Investigation; Formal analysis; Data acquisition and curation A. Chumakov: Methodology; Investigation; Formal analysis; Data acquisition and curation, M. Hanfland: Methodology; Investigation; Formal analysis; Data acquisition and curation. V. Svitlyk: Methodology; Investigation; Formal analysis; Data acquisition and curation. A. D. Rosa: Methodology; Investigation; Formal analysis; Data acquisition and curation.

Funding Open Access funding enabled and organized by Projekt DEAL.

Data Availability Data supporting the findings of this study are available from the corresponding author upon request.

Declarations

Conflict of interest The authors have no conflict of interest to disclose.

References

Angel RJ, Gonzalez-Platas J, Alvaro M (2014) EosFit7c and a Fortran module (library) for equation of state calculations. Z Kristallogr 229(5):405–419. https://doi.org/10.1515/zkri-2013-1711

Anzellini S, Boccato S (2020) A practical review of the laser-heated diamond anvil cell for university laboratories and synchrotron applications. Crystals 10(6):459. https://doi.org/10.3390/cryst10060459

Aprilis G, Strohm C, Kupenko I, Linhardt S, Laskin A, Vasiukov DM, Cerantola V, Koemets EG, McCammon C, Kurnosov A, Chumakov AI, Rüffer R, Dubrovinskaia N, Dubrovinsky L (2017) Portable double-sided pulsed laser heating system for time-resolved geoscience and materials science applications. Rev Sci Instrum. https://doi.org/10.1063/1.4998985

Aprilis G, Kantor I, Kupenko I, Cerantola V, Pakhomova A, Collings IE, Torchio R, Fedotenko T, Chariton S, Bykov M, Bykova E, Koemets E, Vasiukov DM, McCammon C, Dubrovinsky L, Dubrovinskaia N (2019) Comparative study of the influence of pulsed and continuous wave laser heating on the mobilization of carbon and its chemical reaction with iron in a diamond anvil cell. J Appl Phys. https://doi.org/10.1063/1.5067268

Aquilanti G, Pascarelli S, Mathon O, Mũoz M, Narygina O, Dubrovinsky L (2009) Development of micro-XANES mapping in the diamond anvil cell. J Synchrotron Radiat 16(3):376–379. https://doi.org/10.1107/S0909049509007134

Arnoult WJ, Mclellan RB (1972) The solubility of carbon in Rhodium, Ruthenium, Iridium and Rhenium. Scripta Metall 6:1013–1018

Boehler R, De Hantsetters K (2007) New anvil designs in diamond-cells. High Press Res 24(3):391–396. https://doi.org/10.1080/08957950412331323924

Borisov A, Palme H (2000) Solubilities of noble metals in Fe-containing silicate melts as derived from experiments in Fe-free systems. Am Mineral 85(11–12):1665–1673. https://doi.org/10.2138/am-2000-11-1209

Campbell AJ, Danielson L, Righter K, Seagle CT, Wang Y, Prakapenka VB (2009) High pressure effects on the Iron-Iron oxide and Nickel-Nickel oxide oxygen fugacity buffers. Earth Planet Sci Lett 286(3–4):556–564. https://doi.org/10.1016/j.epsl.2009.07.022

Cemic L (2005) Thermodynamics in mineral sciences. In: Thermodynamics in mineral sciences

Cerantola V, Bykova E, Kupenko I, Merlini M, Ismailova L, McCammon C, Bykov M, Chumakov AI, Petitgirard S, Kantor I, Svitlyk V, Jacobs J, Hanfland M, Mezouar M, Prescher C, Rüffer R, Prakapenka VB, Dubrovinsky L (2017) Stability of iron-bearing carbonates in the deep Earth's interior. Nat Commun. https://doi.org/10.1038/ncomms15960

Dorfman SM, Badro J, Nabiei F, Prakapenka VB, Cantoni M, Gillet P (2018) Carbonate stability in the reduced lower mantle. Earth Planet Sci Lett 489:84–91. https://doi.org/10.1016/j.epsl.2018.02.035

Eugster HP (1957) Heterogeneous reactions involving oxidation and reduction at high pressures and temperatures. J Chem Phys 26(6):1761–1762. https://doi.org/10.1063/1.1743626

Fei Y, Ricolleau A, Frank M, Mibe K, Shen G, Prakapenka V (2007) High-pressure geoscience special feature: toward an internally consistent pressure scale. Proc Natl Acad Sci U S A 104(22):9182–9186. https://doi.org/10.1073/pnas.0609013104

Frost DJ (2003) Fe2+ - Mg partitioning between garnet, magnesiowüstite, and (Mg,Fe)2SiO4 phases of the Transition Zone. Am Mineral 88(2–3):387–397. https://doi.org/10.2138/am-2003-2-315

Frost DJ, McCammon CA (2008) The Redox state of Earth's mantle. Annu Rev Earth Planet Sci 36:389–420. https://doi.org/10.1146/annurev.earth.36.031207.124322

Gonzalez-Platas J, Alvaro M, Nestola F, Angel R (2016) EosFit7-GUI: A new graphical user interface for equation of state calculations, analyses and teaching. J Appl Crystallogr 49(4):1377–1382. https://doi.org/10.1107/S1600576716008050

Hirschmann MM (2021) Iron-wüstite revisited: a revised calibration accounting for variable stoichiometry and the effects of pressure. Geochim Cosmochim Acta 313:74–84. https://doi.org/10.1016/J.GCA.2021.08.039

Hirschmann MM, Zhang HL (2023) A revised model for activity-composition relations in solid and molten FePt alloys and a preliminary model for characterization of oxygen fugacity in high-pressure experiments. Eur J Mineral 35(5):789–803. https://doi.org/10.5194/EJM-35-789-2023

Holland TJB, Powell R (1998) An internally consistent thermodynamic data set for phases of petrological interest. J Metamorph Geol 16(3):309–343. https://doi.org/10.1111/j.1525-1314.1998.00140.x

Holland TJB, Powell R (2011) An improved and extended internally consistent thermodynamic dataset for phases of petrological interest, involving a new equation of state for solids. J Metamorph Geol 29(3):333–383. https://doi.org/10.1111/j.1525-1314.2010.00923.x

Huebner JS, Sato M (1970) The oxygen fugacity-temperature relationships of manganese oxide and nickel oxide buffers1 | American Mineralogist | GeoScienceWorld. Am Mineralog J Earth Planet Mater 55(5-6): 934–952. https://pubs.geoscienceworld.org/msa/ammin/article-abstract/55/5-6/934/540688/The-oxygen-fugacity-temperature-relationships-of

Hultgren R, Desai P, Hawkins D, Gleiser M (1973) Selected values of the thermodynamic properties of binary alloys. https://apps.dtic.mil/sti/citations/ADD095435

Jamieson HE, Roeder PL, Grant AH (1992) Olivine-pyroxene-PtFe alloy as an oxygen geobarometer. J Geol 100(1):138–145. https://doi.org/10.1086/629577

Kang SH, Chang SH, Yoo HI (2000) Phase stability of the system Mg–Fe–O. J Solid State Chem 149(1):33–40. https://doi.org/10.1006/JSSC.1999.8490

Kantor I, Prakapenka V, Kantor A, Dera P, Kurnosov A, Sinogeikin S, Dubrovinskaia N, Dubrovinsky L (2012) BX90: A new diamond anvil cell design for X-ray diffraction and optical measurements. Rev Sci Instrum 83(12):125102. https://doi.org/10.1063/1.4768541

Kantor I, Marini C, Mathon O, Pascarelli S (2018) A laser heating facility for energy-dispersive X-ray absorption spectroscopy. Rev Sci Instrum. https://doi.org/10.1063/1.5010345

Komabayashi T, Fei Y, Meng Y, Prakapenka V (2009) In-situ X-ray diffraction measurements of the γ-ε transition boundary of iron in an internally-heated diamond anvil cell. Earth Planet Sci Lett 282(1–4):252–257. https://doi.org/10.1016/j.epsl.2009.03.025

Kurnosov A, Kantor I, Boffa-Ballaran T, Lindhardt S, Dubrovinsky L, Kuznetsov A, Zehnder BH (2008) A novel gas-loading system for mechanically closing of various types of diamond anvil cells. Rev Sci Instrum 79(4):045110. https://doi.org/10.1063/1.2902506

Longo M, McCammon CA, Jacobsen SD (2011) Microanalysis of the iron oxidation state in (Mg,Fe)O and application to the study of microscale processes. Contrib Mineral Petrol 162(6):1249–1257. https://doi.org/10.1007/s00410-011-0649-9

Merlini M, Hanfland M (2013) Single-crystal diffraction at megabar conditions by synchrotron radiation. High Press Res 33(3):511–522. https://doi.org/10.1080/08957959.2013.831088

Miyajima N, Mandolini T, Heidelbach F, Bollinger C (2019) Combining ECCI and FIB milling techniques to prepare site-specific TEM samples for crystal defect analysis of deformed minerals at high pressure. C R Geosci 351(2–3):295–301. https://doi.org/10.1016/j.crte.2018.09.011

Nishihara Y, Nakajima Y, Akashi A, Tsujino N, Takahashi E, Funakoshi KI, Higo Y (2012) Isothermal compression of face-centered cubic iron. Am Mineral 97(8–9):1417–1420. https://doi.org/10.2138/am.2012.3958

O'Neill HSC, Pownceby MI, McCammon CA (2003) The magnesiowüstite: iron equilibrium and its implications for the activity-composition relations of (Mg,Fe)2SiO4 olivine solid solutions. Contrib Mineral Petrol 146(3):308–325. https://doi.org/10.1007/s00410-003-0496-4

O'neill HSC, Wall VJ (1987) The olivine - orthopyroxene - spinel oxygen geobarometer, the nickel precipitation curve, and the oxygen fugacity of the Earth's upper mantle. J Petrology 28(6):1169–1191. https://doi.org/10.1093/petrology/28.6.1169

Pascarelli S, Mathon O, Mairs T, Kantor I, Agostini G, Strohm C, Pasternak S, Perrin F, Berruyer G, Chappelet P, Clavel C, Dominguez MC (2016) The Time-resolved and Extreme-conditions XAS (Texas) facility at the European Synchrotron Radiation Facility: the energy-dispersive X-ray absorption spectroscopy beamline ID24. J Synchrotron Radiat 23:353–368. https://doi.org/10.1107/S160057751501783X

Petrícek V, Dušek M, Palatinus L (2014) Crystallographic computing system JANA2006: general features. Zeitschrift fur Kristallographie 229(5):345–352. https://doi.org/10.1515/zkri-2014-1737

Potapkin V, Chumakov AI, Smirnov GV, Celse JP, Rüffer R, McCammon C, Dubrovinsky L (2012) The 57 Fe synchrotron Mössbauer source at the ESRF. J Synchrotron Radiat 19(4):559–569. https://doi.org/10.1107/S0909049512015579

Prescher C, Prakapenka VB (2015) *DIOPTAS* : a program for reduction of two-dimensional X-ray diffraction data and data exploration. High Press Res 35(3):223–230. https://doi.org/10.1080/08957959.2015.1059835

Prescher C, McCammon C, Dubrovinsky L (2012) MossA: a program for analyzing energy-domain Mössbauer spectra from conventional and synchrotron sources. J Appl Crystallogr 45(2):329–331. https://doi.org/10.1107/S0021889812004979

Rohrbach A, Schmidt MW (2011) Redox freezing and melting in the Earths deep mantle resulting from carbon-iron redox coupling. Nature 472(7342):209–214. https://doi.org/10.1038/nature09899

Rüffer R, Chumakov AI (1996) Nuclear resonance beamline at ESRF. Hyperfine Interact 97–98(1):589–604. https://doi.org/10.1007/bf02150199

Schwerdtfeger K, Zwell L (1968) Activities in solid iridium-iron and rhodium-iron alloys at 1200 C. Trans AIME 242:631–633

Shen W-S, Wu L, Ou T-J, Yue D-H, Ji T-T, Han Y-H, Xu W-L, Gao C-X (2020) A new technology for controlling in-situ oxygen fugacity in diamond anvil cells and measuring electrical conductivity of anhydrous olivine at high pressures and temperatures*. Chin Phys B 29(1):010702. https://doi.org/10.1088/1674-1056/AB5934

Shofner GA, Campbell AJ, Danielson LR, Righter K, Fischer RA, Wang Y, Prakapenka V (2016) The W-WO2 oxygen fugacity buffer (WWO) at high pressure and temperature: implications for fO2 buffering and metal-silicate partitioning. Am Miner 101(1):211–221. https://doi.org/10.2138/am-2016-5328

Solé VA, Papillon E, Cotte M, Walter P, Susini J (2007) A multiplatform code for the analysis of energy-dispersive X-ray fluorescence spectra. Spectrochim Acta Part B Atomic Spectrosc 62(1):63–68. https://doi.org/10.1016/j.sab.2006.12.002

Stagno V, Tange Y, Miyajima N, McCammon CA, Irifune T, Frost DJ (2011) The stability of magnesite in the transition zone and the lower mantle as function of oxygen fugacity. Geophys Res Lett 38(19):1–5. https://doi.org/10.1029/2011GL049560

Stagno V, Ojwang DO, McCammon CA, Frost DJ (2013) The oxidation state of the mantle and the extraction of carbon from Earth's interior. Nature 493(7430):84–88. https://doi.org/10.1038/nature11679

Stagno V, Frost DJ, McCammon CA, Mohseni H, Fei Y (2015) The oxygen fugacity at which graphite or diamond forms from carbonate-bearing melts in eclogitic rocks. Contrib Mineral Petrol. https://doi.org/10.1007/s00410-015-1111-1

Swartzendruber LJ (1984) The Fe-Ir (Iron-Iridium) system. Bull Alloy Phase Diag 5(2):134. https://doi.org/10.1007/BF02868944

Tateno S, Hirose K, Ohishi Y, Tatsumi Y (2010) The structure of iron in earth's inner core. Science 330(6002):359–361. https://doi.org/10.1126/science.1194662

Taylor JR, Wall VJ, Pownceby MI (1992) The calibration and application of accurate redox sensors. Am Miner 77(3–4):284–295

Thompson JB, Waldbaum DR (1969) Analysis of the two-phase region halite-sylvite in the system NaCl-KCl. Geochim Cosmochim Acta 33(6):671–690. https://doi.org/10.1016/0016-7037(69)90114-8

Tomiska J (1989) Massenspektrometrische Ermittlung der thermodynamischen Mischungsgrößen in der kfz-Phase und Berechnung des Schmelzdiagramms Eisen-Palladium / Mass Spectrometric Determination of the Thermodynamic Mixing Properties in the fcc phase and Calculation of the. Int J Mater Res 80(12):888–893. https://doi.org/10.1515/IJMR-1989-801207

Van Aken PA, Liebscher B (2002) Quantification of ferrous/ferric ratios in minerals: new evaluation schemes of Fe L23 electron energy-loss near-edge spectra. Phys Chem Miner 29(3):188–200. https://doi.org/10.1007/s00269-001-0222-6

Van Aken PA, Liebscher B, Styrsa VJ (1998) Quantitative determination of iron oxidation states in minerals using Fe L2,3-edge electron energy-loss near-edge structure spectroscopy. Phys Chem Miner 25(5):323–327. https://doi.org/10.1007/s002690050122

Wirth R (2009) Focused ion beam (FIB) combined with SEM and TEM: advanced analytical tools for studies of chemical composition, microstructure and crystal structure in geomaterials on a nanometre scale. Chem Geol 261(3–4):217–229. https://doi.org/10.1016/J.CHEMGEO.2008.05.019

Woodland AB, O'Neill HSC (1997) Thermodynamic data for Fe-bearing phases obtained using noble metal alloys as redox sensors. Geochim Cosmochim Acta 61(20):4359–4366. https://doi.org/10.1016/S0016-7037(97)00247-0

Yusenko KV, Khandarkhaeva S, Fedotenko T, Pakhomova A, Gromilov SA, Dubrovinsky LS, Dubrovinskaia NA (2019) Equations of state of rhodium, iridium and their alloys up to 70 GPa. J Alloys Compd. https://doi.org/10.1016/j.jallcom.2019.02.206

Zhai S, Ito E (2011) Recent advances of high-pressure generation in a multianvil apparatus using sintered diamond anvils. Geosci Front 2(1):101–106. https://doi.org/10.1016/J.GSF.2010.09.005